Self-induced transparency in a perfectly absorbing chiral second-harmonic generator

Jiankun Hou[1†], Jintian Lin[2†], Jiefu Zhu[3], Guolin Zhao[3], Yao Chen[1], Fangxing Zhang[1], Yuanlin Zheng[3], Xianfeng Chen[3], Ya Cheng[2,4*], Li Ge[5] and Wenjie Wan[1,3*]

[†]Jiankun Hou and Jintian Lin
are Equally contributors

*Correspondence:
Ya Cheng
ycheng@phys.ecnu.edu.cn
Wenjie Wan
wenjie.wan@sjtu.edu.cn

Full list of author information is
available at the end of the article

Abstract

Transparency and perfect absorption are two contradictory terms; a perfect absorber never permits waves to transmit through. However, this statement only remains true in the linear regime, where the nonlinearity has been omitted and the physical system like the perfect absorber is not affected by the incoming waves. Here we experimentally demonstrate an intriguing self-induced transparency effect in a perfectly absorbing optical microcavity, which perfectly absorbs any incoming waves at the low power level, but allows a portion of waves to be transmitted at the higher power due to the nonlinear coupling between the fundamental and its second harmonic modes. Moreover, the asymmetric scattering nature of the microcavity enables a chiral and unidirectional reflection in one of the input ports, this leads to asymmetric and chiral coherent control of the perfect absorption states through phase varying. More importantly, such chiral behaviors also empower the chiral emission of second-harmonic generation with a high distinct ratio in the transparency state. These results pave the way for controllable transparency in a wide range of fields in optics, microwaves, acoustics, mechanics, and matter waves.

Keywords CPA, Microresonator, Self-induced transparency, Chiral, SHG

Introduction

Perfect absorption of the incoming radiation is crucial for many interdisciplinary areas in optics [1, 2], microwaves [3], acoustics[4], mechanics[5], as well as matter waves[6]. One representative example, namely, coherent perfect absorber (CPA) delicately constructs lossy geometry into a cavity design by considering an exact time-reversed laser. This leads to a spectral "blackhole" singularity, a mathematical notion where the system perfectly absorbs any incoming wave without re-emitting [1]. Although firstly proposed and implemented in optics, CPA quickly spans all areas of classical wave systems from microwave to acoustics[1–6]. More importantly, CPA promises a wide range of practical applications in optical information processing[7], energy harvesting[8], photo-detection[9], and sensing[10].

Transparency and perfect absorption seem to be a paradox at the first glance, a *perfect* absorber never permits waves to transmit through. However, this is mainly because

most of the prior works are implemented in the linear regime, i.e. incoming waves do not affect the perfect absorber itself. Contrarily, waves' amplitude can greatly alter the dynamics of absorption in the nonlinear regime, which is more universal and common in real physical systems. A nonlinear version of CPA has been theoretically studied [11], but only limited to their nonlinear dynamics. Such devices are usually composed of a sandwich structure with an embedded nonlinear absorbing layer, which creates an extra obstacle to meet the CPA condition. For example, nonlinearity leads to a self-induced perfect absorption above a certain critical value with microwave [12]; And the CPA of nonlinear matter waves in an atomic Bose-Einstein condensate can be achieved easier than its linear analogs because of the strength of two-body interaction nonlinearity [6]. Hence, transparency can be much anticipated, though no experimental observation yet, in a nonlinear version of CPA.

On the other hand, transparency indeed can be achieved through an *externally* controlled manner in an opaque /absorbing medium. In atomic physics, electromagnetically induced transparency (EIT) allows the flipping of an optical opaque window to a transparent one under a *secondary* coherent illumination beam even at the few-photon limit[13]. This process provides tremendous opportunities for quantum physics and information science, enabling applications in all-optical and quantum information processing, slow/fast light, and photon storage[13–16]. Later, by recognizing the interference effect as the key working mechanism behind EIT, classical analogies that mimic the EIT effect are under active pursuit in various physical systems, including microresonators[7, 17–19], photonic crystals[20], and plasmonic metamaterials[21]. However, these works still rely on the external-control mean such as a second laser. Meanwhile, self-induced transparency has been extensively studied mainly in atomic systems, thanks to the strong nonlinearity of atoms [22, 23], but the associated cooling and vacuum systems halt their practical applications. So far, self-induced transparency in a perfect absorbing optical cavity has never been reported till this work.

In this work, we experimentally demonstrate a self-induced transparency effect in a perfectly absorbing optical microcavity, which only totally absorbs low-power incoming waves in the linear regime, but dramatically turns into a partial transparency state after ramping up the input power. Such self-induced transparency is introduced by the nonlinear coupling between the optical modes at the fundamental frequency and its second harmonic, causing partially breaking the balance condition of a coherent destructive interference which holds the key to enabling perfect absorption or critical coupling initially in the microcavity. Furthermore, we find the current microcavity device contains a unique asymmetric scattering feature of chiral and unidirectional reflection, which is caused by multiple surface scatters that break the chiral symmetry. As a result, asymmetric and chiral coherent control of the perfect absorption states is realized through phase varying. This coherent control can be further extended into the second harmonic spectrum, resulting in a chiral emission of second-harmonic generation with a high distinct ratio in the transparency state. These results should be general and universal among other physical systems with nonlinearity like microwaves, acoustics, mechanics, and matter waves, hence it paves the way for practical applications in all-optical signal processing and quantum information.
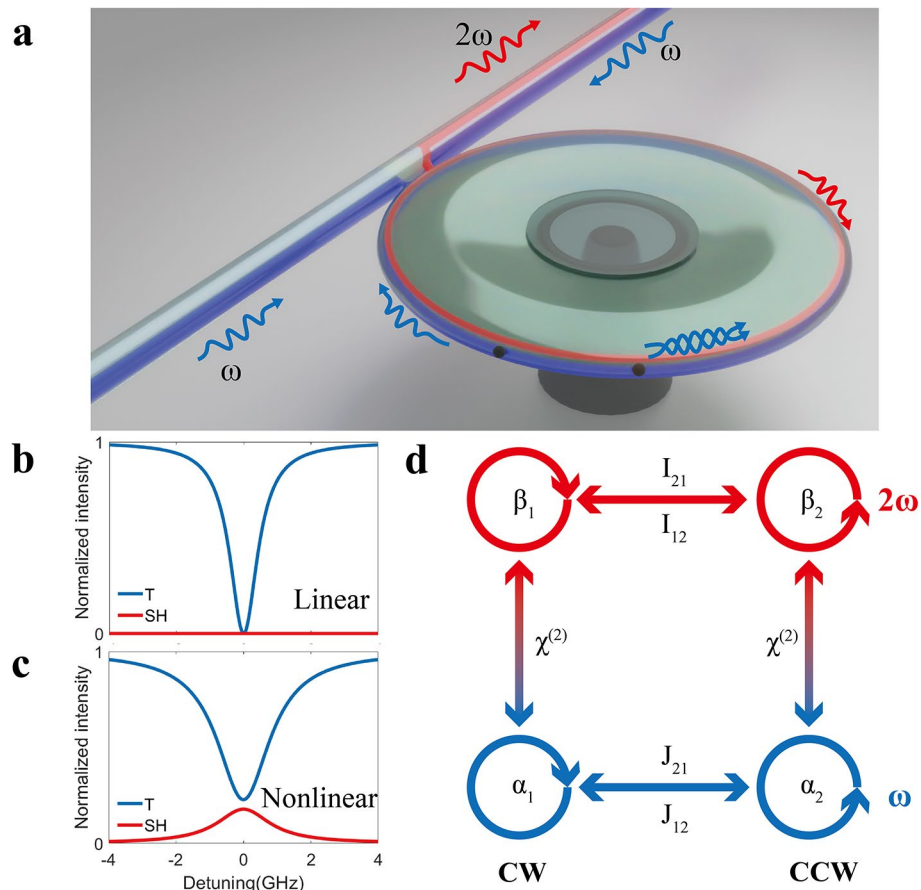
Fig. 1 Illustration of self-induced transparency in a perfectly absorbing optical microcavity. (**a**) Schematic of a tapered fiber coupled lithium niobate microcavity with quadratic nonlinearity, where one-port input is perfectly absorbed inside the microcavity at (**b**) the critical coupling point (theoretical results). Loss factors consist of linear scattering, material absorption, and nonlinear loss through second harmonic generation, which breaks the perfect absorption state and leads to self-induced transparency in (**c**). (**d**) Moreover, the situation becomes more complex when both ports are excited by the fundamental waves α_1(CW) and α_2(CCW) and their second harmonic waves β_1(CW) and β_2(CCW) through the second-order nonlinearity $\chi^{(2)}$. The optical waves in each direction are coupled through the linear scattering processes, i.e., J_{12}/J_{21} and I_{12}/I_{21}

Results and discussion

The original CPA idea composes of two ports geometry to enable perfect absorption in the embedded layer by coherent destructive interference[2]. One-port CPA can also be realized in a waveguide coupled microcavity scheme (Fig. 1a), in which similar destructive interference between the cavity's out-coupling light & the residual transmission, also known as critical coupling[24]. This leads to complete and perfect absorption of input waves inside the microcavity, where light energy dissipates in the form of material absorption and surface scattering, while the in-coupling portion from the waveguide is exactly balanced by the out-coupling port from the cavity. At this equilibrium state, any perturbation breaking this balance can lead to the disappearance of a perfect absorption state. In the linear regime (Fig. 1b), the incoming waves can hardly disturb the system at low power, in contrast, high-power inputs can trigger the nonlinear response of the system such that the dedicated balance of input and output will be destroyed, resulting in self-induced transparency in the transmission spectrum (Fig. 1c).

One representative example of such is a microcavity of quadratic second-order nonlinearity, which allows the second harmonic generation (SHG) from the fundamental wave (FW) frequency ω of the incoming waves to its second harmonic 2ω. With a higher input power, a portion of input optical energy is converted into its second harmonic, effectively creating a "nonlinear loss" at the fundamental frequency. As a result, the aforementioned most important balance will be broken, destructing the perfect absorption at ω (Fig. 1c). More specifically, we consider a tapered fiber coupled microcavity with second-order nonlinear susceptibility $\chi^{(2)}$ and internal coupling between clockwise (CW) and counterclockwise (CCW) directions (Fig. 1d), and the evolution dynamics can be described by four sets of coupled rate equations, each at ω and 2ω, and in both CW/CCW directions. The governing Hamiltonian is given by $i\frac{d\psi}{dt} = H\psi$, where $\psi = (\alpha_1, \alpha_2, \beta_1, \beta_2)^T$ represents field vectors, and $\alpha_1, \alpha_2, \beta_1, \beta_2$ are the internal cavity amplitudes for CW, CCW waves at ω, CW, CCW waves at 2ω, respectively. H is a 4×4 non-Hermitian Hamiltonian:

$$H = \begin{pmatrix} -\Delta_1 - i\gamma_{10} & -J_{12} & -2g^*\alpha_1^* & 0 \\ -J_{21} & -\Delta_1 - i\gamma_{10} & 0 & -2g^*\alpha_2^* \\ -g\alpha_1 & 0 & -\Delta_2 - i\gamma_{20} & -I_{12} \\ 0 & -g\alpha_2 & -I_{21} & -\Delta_2 - i\gamma_{20} \end{pmatrix} \tag{1}$$

where the resonant frequency detuning terms are $\Delta_1 = (\omega - \omega_1)$ at the fundamental frequency, $\Delta_2 = (2\omega - \omega_2)$ at its second harmonic; for each frequency, $\gamma_{10} = (\gamma_1 + \gamma_{c1})/2$, $\gamma_{20} = (\gamma_2 + \gamma_{c2})/2$ are the effective loss, and γ_{c1}, γ_{c2} represent the coupling strength with which the cavity coupled to the waveguide; γ_1, γ_2 are the intrinsic loss terms which are dominated by material absorption and surface impurities; g is the second-order nonlinear coupling strength constant determined by $\chi^{(2)}$. The coupling terms J_{12}/J_{21} and I_{12}/I_{21} between CW/CCW modes at ω and 2ω, respectively, arising from linear scattering. Note that, H is a *nonlinear* Hamiltonian as well, whose off-diagonal terms, e.g. $-2g^*\alpha_1^*$, $-2g^*\alpha_2^*$, depending on the internal fields α_1, α_2. This is *the origin* of self-induced transparency.

For a unidirectional input, i.e. $\alpha_2 = 0$, we can simplify H into a 2×2 matrix in supplement S1. Under the steady-state assumption, we can solve the associated coupled rate equations and obtain the transmission rate:

$$T = \left| 1 + \frac{\gamma_{c1}}{i\Delta_1 - \frac{\gamma_1 + \gamma_{c1}}{2} + \frac{2|g|^2|\alpha_1|^2}{i\Delta_2 - \frac{\gamma_2 + \gamma_{c2}}{2}}} \right|^2 \tag{2}$$

and the intra-cavity second harmonic amplitude is given by:

$$\beta_1 = -\frac{ig\alpha_1^2}{i\Delta_2 - \frac{\gamma_2 + \gamma_{c2}}{2}} \tag{3}$$

In the linear case, i.e. $\alpha_1 \to 0$, Eq. 2 perfectly represents a scenario for single-port CPA, where the critical coupling occurs at $\gamma_{c1} = \gamma_c$ [24]. The corresponding transmission spectra exhibit a perfect absorbing dip, i.e. $T = 0$ at the zero detuning point $\Delta_1 = 0$ in Fig. 1b. Nonlinearly, when increasing the signal amplitude α_1, the CPA dip will diminish, allowing a portion of the light to be transmitted, termed as self-induced transparency (Fig. 1c). Note that, only the income wave signal amplitude has been increased during
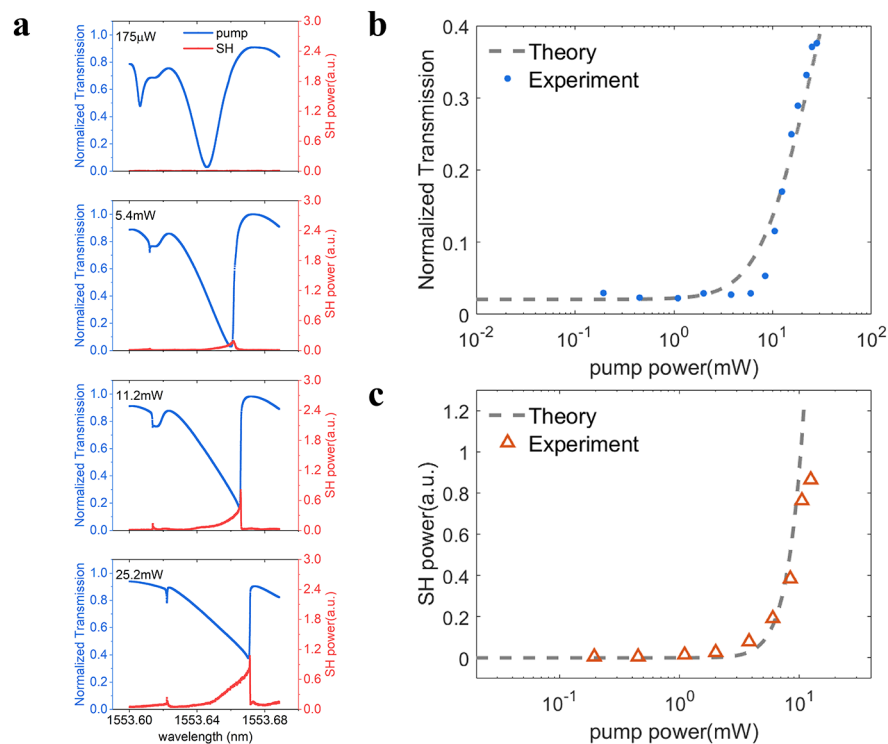
Fig. 2 Experimental observation of self-induced transparency in a one-port perfect absorber. (**a**) Experimentally measured transmission spectra of the input pump (blue) and its SHG (red) at various pump power. Self-induced transparency manifests itself at the higher pumping (bottom), in contrast to the perfect absorption state at the lower pumping (top). The corresponding transmission rate of the input pump (**b**) and the SHG power (**c**) are measured with respect to the pump power, both exhibit quadratic dependences due to the second-order nonlinearity

this process, it is a self-induced action of signal amplitude in contrast to the linear case at a lower amplitude level. In the meantime, the microcavity starts to generate the second harmonics of the fundamental waves given by Eq. 3, effectively becoming a second-harmonic generator. Moreover, such SHG is resonantly enhanced due to the resonances of the microcavity (Fig. 1c).

In our experiment, a microcavity (Q-factor $\sim 10^6$) with second-order nonlinearity is fabricated on a lithium niobate on insulator (LNOI) platform [Details in the method section, 25]. As shown in Fig. 1a, the microcavity with a diameter $\sim 100\,\mu m$ is coupled with a tapered fiber within which a laser source around the 1550 nm telecommunication band propagates. The laser signals can be launched into both ports of the fiber, which also serve as the output ports for monitoring both the linear transmission and the SHG output on both ports. By slowing scanning the tunable laser at a speed of 0.01 nm/s through the resonances from the red-detuned region, transmission spectra can be obtained in Fig. 2. The tapered fiber is precisely positioned on a piezoelectric stage to tune the gap (~ 100 nm) from the cavity with ~ 10 nanometers resolution, such that careful positioning of the tapered fiber can reach the critical coupling condition in Fig. 2a. Note that, due to the surface scattering from dust, scatter or surface roughness, the CW resonances can be effectively coupled with its counterpart, i.e. counterclockwise (CCW) modes, both at ω and 2ω as shown in Fig. 1d. This coupling mechanism dramatically complicates the dynamics both in the linear regime and nonlinear one, enabling some intriguing effects

like unidirectional reflection and chiral SHG, we shall soon discuss them in the following section.

Under this one-port excitation scheme, we experimentally observe a perfect absorption dip with ~99% efficiency in the transmission spectrum at the critical coupling condition as shown in Fig. 2a. The incident power of the laser is measured to be ~175μW, no SHG is visible at such low power. As the pump laser's power is gradually tuned up, starting around several milliwatts, a clear SHG signal is detected in the through-port, indicating the energy flow from the fundamental modes to its second harmonics. As a result, the absorption dip begins to reduce in the transmission spectrum. Figure 2b shows such transmission can raise up from almost none to ~40% when the pump laser reaches 25.2mW, a sharp contrast to its behavior in the linear regime at low power. This nonlinear dynamic marks self-induced transparency in the one-port CPA configuration, only depending on the input laser's power. In the meantime, the SHG signal is also increasing quadratically in Fig. 2c according to the theory in Eq. 3. Moreover, the on-resonance transmission T will grow slowly at high pump power and approach 1 when the input power is infinity, which can be easily deduced from Eq. 2. Note that, the original Lorentz lineshape in the linear case is greatly distorted into a triangled one due to the thermal-pulling effect [26], but this behavior only shifts the resonances horizontally along the frequency axis, not their transmission [see supplementary S7].

Traditional CPAs are featured with a two-port apparatus for active phase control of the perfect absorption state[2], where coherent control of the relative phases between the two input ports can actively switch between the CPA and the maximum scattering state, or even lasing mode[27]. Given the tapered fiber coupling scheme, it is also possible for us to launch two beams simultaneously from both ports into the microcavity, in which the surface scatters can couple the waves in both directions together, represented in the off-diagonal terms in Eq. 1, e.g. J_{12}, J_{21}. In Fig. 3, near a critical coupling condition from a left excitation (Fig. 3a), a near-zero transmitted dip is observed in the transmission, this is companied by a strong reflection to the left, indicating a big scattering factor from CW to CCW mode, i.e. J_{21}. In a contrast to the right excitation case, a transmission dip with a similar efficiency of ~95% is observed, but with a much lower back-scattered light to the right port. The similarity between the two transmission spectra is guaranteed by the optical reciprocity [28], while the unequal backscattering arises from the asymmetric scatter distribution inside the cavity. For example, in the inset of Fig. 3a, we do observe two strong out-plane scattering signals from the right corner of the microcavity.

Such chiral behaviors, i.e. CPA from both directions and unidirectional reflector, originate from the important fact that the backscattering between intracavity CW and CCW traveling waves is asymmetric, i.e. $J_{12} \neq J_{21}$[29, 30], which introduces asymmetric reflection output from the scattering matrix (S-matrix) [31]. Intuitively, this process could be understood as a linear interference between two scattering waves from two scatters at the coupling point, the two scatters have to be distinct in terms of their scattering coefficients to break the chirality [29]. Previously, this very idea has been testified to realize chiral modes and directional lasing at exceptional points in a microcavity[32]; More recently, CPA on an exceptional surface with a chiral reflection has also been demonstrated with a mirror coupled microcavity device[33]. Our fabricated microcavity naturally contains such asymmetrical surface scattering properties due to fabrication
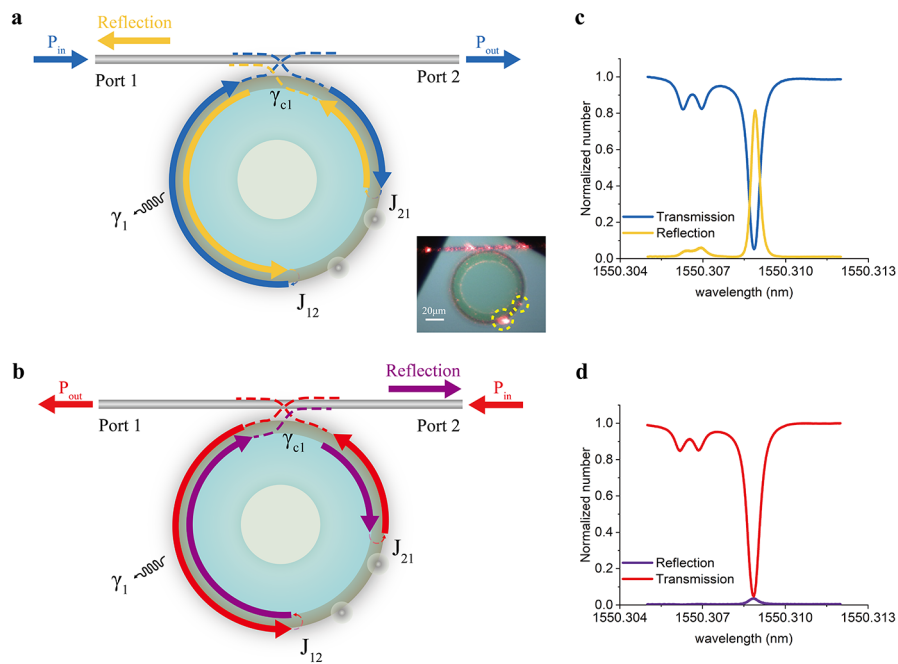
Fig. 3 Unidirectional reflector in a one-port perfect absorber. (**a**) and (**b**) Schematic diagrams of unidirectional reflectors in a one-port perfect absorber with an incident beam from left and right ports, respectively. γ_1 : scattering loss, γ_{c1} : coupling rate. The linear coupling rates between CW and CCW are not equal in the current case, i.e. $J_{12} \neq J_{21}$ in the current microcavity. Inset in (**a**): top-view picture of the microcavity device. (**c**) and (**d**) Their corresponding transmission and reflection spectra from left and right, respectively, show the same transmission from both ports, but two distinguished reflection spectra

defects or external dust as shown in Fig. 3a, it enables us to observe for the first time, to our knowledge, such chiral behaviors of CPA in a single microcavity.

This chiral behavior of the one-port CPA has its consequences in its two-port version, especially in the coherent control of the CPA. In the classical two-port CPA experiment, the symmetric lossy cavity ensures the total destructive interferences between the transmitted and reflected beams, simultaneously on both the incident ports. This leads to the perfect absorption only inside the lossy layer[2]. This requires a pair of symmetric equal-amplitude incident waves from both sides. However, when such symmetry is broken, for example, with a parity-time symmetric cavity[27], the required ratio between the two ports is not unit anymore. To demonstrate the coherent control of two-port CPA, we launch two beams with unequal power from both ports into the microcavity at the aforementioned critical coupling condition (Fig. 4a). As usual, both transmission spectra under single-port excitation exhibit well complete absorption dips in Fig. 4b, while their corresponding reflection spectra differ by 20dB. In Fig. 4b, by comparing the output spectra from Port 1 (reflection of α_{in1} and transmission of α_{in2}) and Port 2 (reflection of α_{in2} and transmission of α_{in1}), we can find an optimal spectral point to achieve complete destructive interference when implementing phase control, a similar technique has been used in the original two-port CPA experiment[2].

In the linear regime (low power, no SHG), we observe large power variations from both ports during the phase varying process. Similar to prior works, a complete destructive cancellation of the Port 1's output is evident in Fig. 4c & g, at which the reflection of α_{in1} and the transmission of α_{in2} are equal in amplitude (Fig. 4b) and completely out of phase at the π phase difference. As a result, Port 1 can be actively switched on and
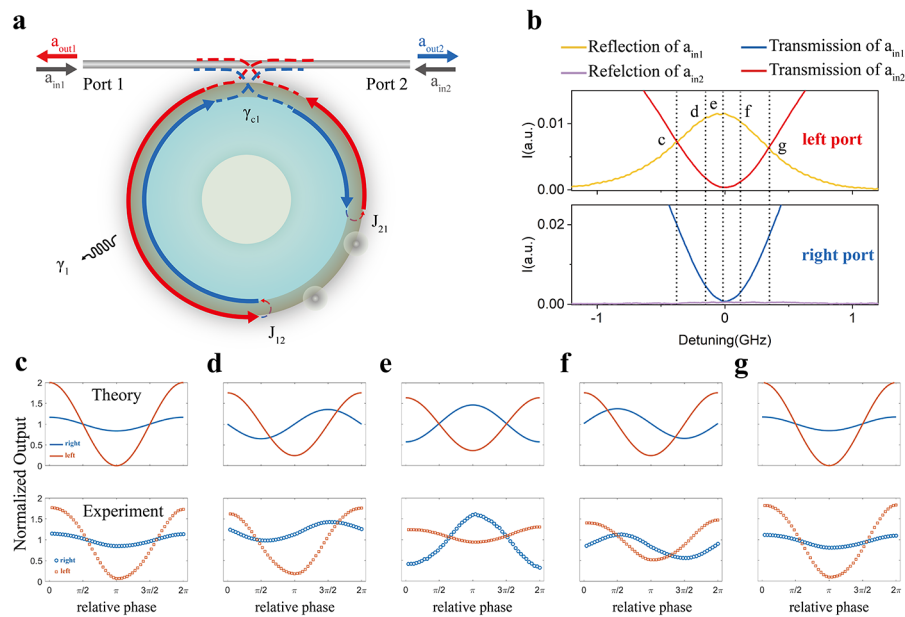
Fig. 4 Coherent control of a two-port chiral absorber. (**a**) Schematic diagram of the original one-port perfect absorber, but with two equal input beams from both ports. As a result of scatters that break the chiral symmetry, the CW and CCW are coupled together, hence affecting the output dynamics of both ports. (**b**) Output spectra of left (upper) and right (lower) ports, in which, the reflection of α_{in1} (yellow) and α_{in2} (purple), the transmission of α_{in1} (blue) and α_{in2} (red) are depicted separately. Five representative cases of phase modulation results (top: theory, bottom: experiment) are shown in (**c**)-(**g**) with various frequency detuning Δ_1 of -0.341 GHz, -0.127 GHz, 0, 0.127 GHz, 0.341 GHz, respectively. The incident power of fundamental waves from left and right ports are controlled precisely by a variable optical attenuator such that the reflection of α_{in1} and the transmission of α_{in2} can coincide at points c and g in (**b**). Port 1 input beam: 16μw. Port 2 input beam: 7.5μw. When both ports are excited, chiral perfect absorption can be observed in the left port, (**c**) & (**g**) due to the complete destructive interference cancellations, meanwhile, there are some remaining transmissions in the right port. The parameters used in the simulation are obtained by fitting the spectrum in (**b**): $\gamma_{c1} = 0.6097265$GHz, $\gamma_1 = 0.8772764$GHz, $J_{21} = 0.34$GHz, $J_{21} = 0.05$GHz

off purely by phase control. Meanwhile, the output power fluctuation of Port 2 is much milder during the phase varying, simply due to the unequal contributions of the incident waves from both ports. Such chiral behaviors are universal among the other spectral positions, e.g. Figure 4d-f, where the phase varying does lead to power fluctuations in both ports, but in a synchronous manner. Contrarily, complete destructive cancellations can only be observed in the spectral position depicted in Fig. 4c,g, not others. Particularly, the zero-detuning point, i.e. Figure 4e, is the CPA point in the original symmetric setup in prior work [2], however, this is not the case in the current setup due to the unbalanced reflection and transmission. These experimental observations also match well with the theoretical results calculated using Eq. 1. as shown in Fig. 4c-g [supplement S2]. If we increase the input power into the nonlinear regime, the nonlinear loss should be considered, chiral complete absorption will be broken at c&g points[see supplement S4]. Furthermore, we have theoretically proposed a coherent control of such two-port chiral CPAs, which are capable of fully absorbing incident waves from both ports [supplement S3]. But this requires some dedicated design parameters, such as loss factors, not feasible in the current experiments, we will leave it for further investigation.

More interestingly, this chiral dynamic can be translated into a nonlinear regime, a phase-controllable chiral second harmonic generation can be directly observed as the result of its interference between CW and CCW mode at the FW frequency. It is well-known that the
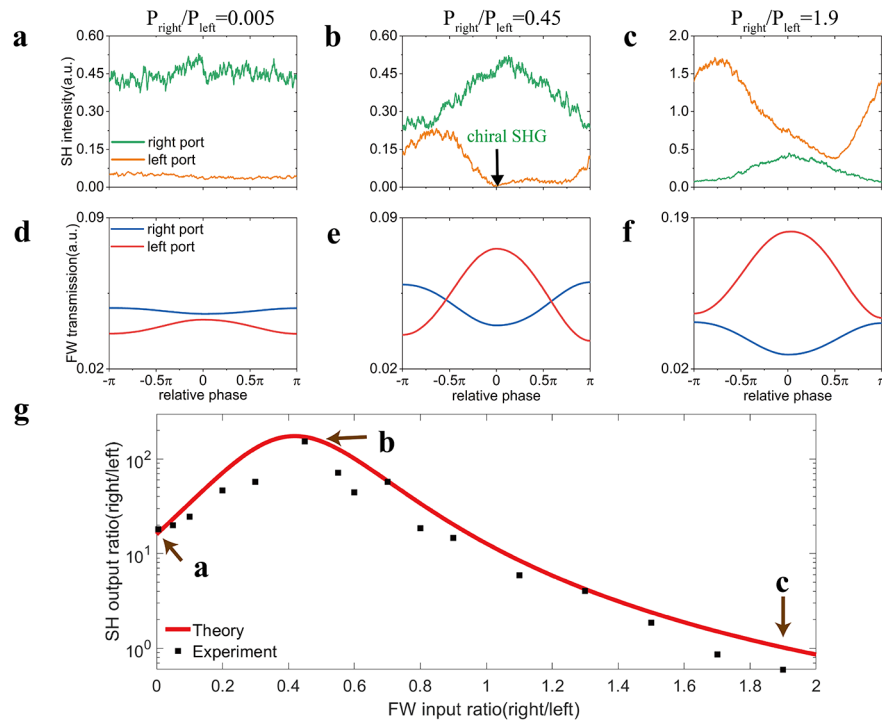
Fig. 5 Chiral second harmonic generation through coherent control. Three typical phase-controllable SHG with different input power ratios between right and left ports are shown in (**a**) to (**c**), with their corresponding fundamental waves' output from the two ports (**d**) to (**f**). All of the results are measured at the zero-detuning point ($\Delta_1 = 0$). The perfect annihilation of left SHG occurs in (**b**), when the two fundamental wave inputs are in-phase (**e**). Such distinction ratio of SHG outputs from both ports are plotted against the fundamental wave input ratio between the right and left in (**g**), which shows an optimal point with a maximal distinction ratio of ∼153 at $P_{right}/P_{left} = 0.45$. The power of the left-input beam is fixed at 1mW while varying the right one to change the input power ratio

SHG has to be restricted into a well-defined direction due to the phase-matching condition. In the case of the one-port nonlinear CPA shown above, the induced SHG is in the forward direction, the same as its pump beam at the fundamental frequency (Fig. 2). Under the two-port illumination (Fig. 4), the SHG in both CW and CCW directions can intermix directly with each other due to the presentence of surface scattering, i.e. I_{12}/I_{21} in Eq. 1, or in an indirect manner, the CW/CCW modes of fundamental waves intermix first through J_{12}/J_{21}, then affect their SHGs [see supplementary S4]. Effectively, this also creates a two-path quantum interferences scheme in Fig. 1d, a very important route for coherent quantum control [34]. In the current study, we find the second indirect route domain, especially when the SHG signals are relatively weak with a low conversion efficiency of ~0.1%. We still observe the coherent control SHG signals from both output ports due to the phase varying of their fundamental waves in Fig. 5.

Fig. 5a-c shows several typical cases of the phase-controlled SHGs with multiple CW/CCW pump intensity ratios. All the results are measured at the zero-detuning point of the fundamental waves, i.e. $\Delta_1 = 0$, at which the incident beams with various intensity ratios P_{right}/P_{left} are scanned in their relative phases from $-\pi$ to π. Here the input power is kept under 1mW to avoid any thermal-induced waveform distortion. When the P_{right}/P_{left} ratio is low, i.e. the dominated input is launched into the CW modes through the left port, only small intensity variations are observed both at$_\omega$ and 2ω (Fig. 5a,d). In sharp contrast, much larger modulations are visible in both phase spectra

when $P_{right}/P_{left} = 0.45$. Particularly, a total annihilation point of SHG is observed in the CCW modes at the zero phase delay (Fig. 5b), when most of SHG occurs in a chiral manner in the other CW direction. This is caused by the destructive interference between the two in-phase incident beams at ω (Fig. 5e). Note that, the power ratio is not one, which is a prerequisite condition for a linear total destructive interference. Here it is mainly due to the asymmetrical scattering as mentioned above. Moreover, we notice unsynchronized phase modulations by comparing the two frequency spectra at ω and 2ω, this is caused by the nature of nonlinear second harmonic processes in which two fundamental photons are converted into one single second-harmonic photon, hence their phases are not synchronized[detailed theoretical calculation in the supplement]. With a higher ratio, i.e. $P_{right}/P_{left} = 1.9$, we observe a reversal direction of SHG to the CCW direction when the incident waves are in-phase, but the SHGs in both directions tend to be equal at a phase difference of $\pi/2$. To demonstrate the chirality of SHGs during the phase modulation, we plot the distinction ratio of SHGs between the CW and CCW directions as opposed to the power ratio P_{right}/P_{left} in Fig. 5 g. An optimal contrast point is evident near $P_{right}/P_{left} = 0.45$ with a distinction ratio over 100 times (Fig. 5b), meaning SHGs are highly directional in the CW direction. Moving to either side, such distinction ratio diminishes. These results offer an attractive tool for unidirectional SHG and coherent controlled nonlinear processes in the future [35]. In addition, according to previous studies, we can use two nanotips introduced in the mode volume as two scatters[36] or etch holes in the microring[37] to break the chiral symmetry. Therefore, designing an asymmetric cavity for a second-harmonic generation with a high distinct ratio in the transparency state is feasible.

Conclusion

In summary, we experimentally demonstrate a self-induced transparency effect in a perfectly absorbing optical microcavity-based second harmonic generator, which is capable of perfectly absorbing incoming waves in the linear regime, but turns into a transparency state and begins to emission second harmonics in a coherent controlled chiral manner. There are a few possible impacts on the optics fields and quantum physics. For example, the signature self-induced transparency may partially resemble the nonlinear behavior of an electrical diode, a building block for the integration circuits (IC). Similar to the forward-biased scenarios of the electrical diode, the signal transmission is relatively low with a small biased voltage, but nonlinearly and drastically increases with a larger voltage. Our device may serve as an optical version of the diode. The second feature of coherent controllable and chiral transparency may offer another opportunity for all-optical switching, just like its counter electrical transistors in IC. Moreover, the chiral emission of SHG is also an attractive platform for optical frequency conversion applications, in which the SHG usually co-propagates with its pump beam due to the phase-matching condition. Here in our device, we may specifically design the output port of the SHG, which may/may not align with its pump depending on the coherent control. At last, we believe these results are universal across multidiscipline in microwaves, acoustics, mechanics, and matter waves, hence it paves the way for practical applications of coherent control and nonlinear induced transparency in information processing and frequency conversion.

Methods

Sample fabrication

The micro-disk resonator (~100 μm diameter) is fabricated with femtosecond laser direct writing and the chemical-mechanical(CM) polishing [38] in four steps. First, a thin layer of chromium (Cr) is deposited on the surface of the LNOI through thermal evaporation coating, then space-selective femtosecond laser direct writing is used to pattern the Cr film into a circular disk, next, CM polishing is significant for improving the surface smoothness, leading to high Q-factor, finally, removing the SiO2 buffer layer and the Cr thin film with two consecutive chemical wet etching processes. The thickness of the sidewall of the microcavity is 900 nm and the typical Q factor is about 10^6, which leads to very strong local field strength. The tapered fiber is made of the standard single-mode fiber (G.652.D) and is melted by oxyhydrogen flame. In the coupling region, the tapered fiber is 2~3 μm in diameter and is in contact with the micro-disk resonator for stability during the whole experiment.

Experimental details

A continuously tunable laser (CTL, Toptica Photonics) with a center wavelength of 1550 nm is used as the optical source. The optical source is amplified by an EDFA and divided into two branches (CW and CCW) by the coupler (50:50). The intensity and polarization of the CW branch are controlled by the variable optical attenuator (VOA) and polarization controller (PC). The other branch (CCW) is modulated by an electro-optic modulator (EOM) to vary relative phase between two branches. Two power meters are used to monitor the input power of each branch[see Supplementary S5], Once the pump is detuned at the required frequency, the relative phase is changed by EOM using an external control signal.

Fundamental and second-harmonic signal detection

The SH signal is detected by a photomultiplier tube (PMT, CR114) connected to an OSA and the transmission spectra of each branch are detected by two PDs (DET02AFC) [see Supplementary S5]. There is no need to use the filter in this system. Because the PMT does not respond to the 1,550 nm communication band and the response band of DET02AFC is 800-1700 nm, not including 775 nm. The SH signal is detected from the 1×2 coupler (50:50) and the transmission signal of the pump is detected from a 2×2 coupler (10:90) through 10% end in each branch. The external control signal is a triangular wave with 20 Vpp and 1 kHz frequency and was used as a trigger source in OSA during this experiment.

Critical coupling and perfect absorption condition

Critical coupling occurs when the external lifetime is matched to the intrinsic cavity decay rate $\left(\tau_{ex}^{-1} = \tau_0^{-1}\right)$ i.e. the coupling strength between waveguide and microcavity is equal to the intrinsic loss of the cavity $\gamma_{c1} = \gamma_1$. In this case, the transmission past microcavity vanishes, and entire power is transferred from the optical wave to the cavity modes. The transmission vanishes due to the interference of the cavity leakage field and transmitted pump field, which exhibit equal magnitude but a relative phase shift π. This completely destructive interference is also called perfect absorption. To achieve perfect absorption, it is necessary to appropriately choose the values of the system parameters, such as the gap distance between waveguide and cavity, the scattering strength. In addition, the intensities and relative phases of the input beams are significant as well. In our experiment, we accurately control the coupling strength γ_{c1} by a 3-axis nano-translation stage (Thorlabs, MDT630B). We first set the

gap distance between waveguide and cavity equal to 500 nm, then reduce the distance slowly, until reaches critical coupling condition.

Phase control

The total relative phase is defined as $(\varphi_2 - \varphi_1 - \pi/2 - \Delta\phi)$ is influenced by two factors [see supplementary S2]. One is the constant phase results from the structure of the system, which determines the output intensity relationship between two ports (Fig. 4c-f). This phase is related to the coupling strength γ_{c1}, intrinsic loss of the cavity γ_1 and the detuning Δ_1. In this experiment, the coupling condition is fixed, so we change the constant phase by varying Δ_1. The other is phase difference $(\Delta\phi)$ between two branches, controlled through EOM. The range of $\Delta\phi$ is from 0 to 2π scanned by an external triangle signal source (1 kHz,20Vpp). The output intensity changes as the relative phase changes due to interference.

Abbreviations

CPA   Coherent perfect absorber.
EIT   electromagnetically induced transparency.
SHG   Second harmonic generation.
FW   Fundamental wave.
CW   clockwise.
CCW   counterclockwise.
IC   integration circuits.

Supplementary Information

The online version contains supplementary material available at https://doi.org/10.1186/s43074-022-00068-y.

Supplementary Material 1

Declarations

Competing interests

The authors declare that they have no competing interest.

Author details

[1]State Key Laboratory of Advanced Optical Communication Systems and Networks, University of Michigan-Shanghai Jiao Tong University Joint Institute, Shanghai Jiao Tong University, 200240 Shanghai, China
[2]State Key Laboratory of High Field Laser Physics, Shanghai Institute of Optics and Fine Mechanics (SIOM), CAS Center for Excellence in Ultra-Intense Laser Science, Chinese Academy of Sciences (CAS), 201800 Shanghai, China
[3]Department of Physics and Astronomy, Shanghai Jiao Tong University, 200240 Shanghai, China
[4]School of Physics and Electronic Science, East China Normal University, 200241 Shanghai, China
[5]Department of Physics and Astronomy, College of Staten Island, the City University of New York, 10314 New York, USA

References

1. Chong YD, Ge L, Cao H, Stone AD. Coherent perfect absorbers: time-reversed lasers. Phys Rev Lett. 2010;105:053901.
2. Wan W, Chong YD, Ge L, Noh H, Stone AD, Cao H. Time-reversed lasing and interferometric control of absorption. Science. 2011;331:889–92.
3. Landy NI, Sajuyigbe S, Mock JJ, Smith DR, Padilla WJ. Perfect metamaterial absorber. Phys Rev Lett. 2008;100:207402.
4. Mei J, Ma G, Yang M, Yang Z, Wen W, Sheng P. Dark acoustic metamaterials as super absorbers for low-frequency sound. Nat Commun. 2012;3:756.
5. Ma G, Yang M, Xiao S, Yang Z, Sheng P. Acoustic metasurface with hybrid resonances. Nat Mater. 2014;13:873–8.
6. Andreas M, Bodhaditya S, Christian B, Jian J, Jens B, Ralf L, Zezyulin DA, Konotop VV, Herwig O. Coherent perfect absorption of nonlinear matter waves. Sci. Adv. 2018;4:8.
7. Zheng Y, Yang J, Shen Z, Cao J, Chen X, Liang X, Wan W. Optically induced transparency in a micro-cavity. Light Sci Appl. 2016;5:e16072.
8. Kats MA, Capasso F. Optical absorbers based on strong interference in ultra-thin films. Laser Photon Rev. 2016;10:735–49.
9. Konstantatos G, Sargent EH. Nanostructured materials for photon detection. Nat Nano. 2010;5:391–400.
10. Liu N, Mesch M, Weiss T, Hentschel M, Giessen H. Infrared perfect absorber and its application as plasmonic sensor. Nano Lett. 2010;7:2342–8.
11. Mostafazadeh A. Nonlinear spectral singularities for confined nonlinearities. Phys Rev Lett. 2013;110:260402.
12. Suwunnarat S, Tang Y, Reisner M, Mortessagne F, Kuhl U, Kottos T. Non-linear coherent perfect absorption in the proximity of exceptional points. Commun Phys. 2022;5:5.
13. Boller KJ, Imamoğlu A, Harris SE. Observation of electromagnetically induced transparency. Phys Rev Lett. 1991;66:2593–6.
14. Harris SE, Yamamoto Y. Photon switching by quantum interference. Phys Rev Lett. 1998;81:3611–4.
15. Hau LV, Harris SE, Dutton Z, Behroozi CH. Light speed reduction to 17 metres per second in an ultracold atomic gas. Nature. 1999;397:594–8.
16. Phillips DF, Fleischhauer A, Mair A, Walsworth RL, Lukin MD. Storage of light in atomic vapor. Phys Rev Lett. 2001;86:783–6.
17. Zhang F, Feng Y, Chen X, Ge L, Wan W. Synthetic anti-PT symmetry in a single microcavity. Phys Rev Lett. 2019;124:053901.
18. Qin T, Yang J, Zhang F, Chen Y, Shen D, Liu W, Chen L, Jiang X, Chen X, Wan W. Fast-and slow-light-enhanced light drag in a moving microcavity. Commun Phys. 2020;3:118.
19. Xu Q, Sandhu S, Povinelli ML, Shakya J, Fan SH, Lipson M. Experimental realization of an on-chip all-optical analogue to electromagnetically induced transparency. Phys Rev Lett. 2006;96:123901.
20. Yanik MF, Suh W, Wang Z, Fan SH. Stopping light in a waveguide with an all-optical analog of electromagnetically induced transparency. Phys Rev Lett. 2004;93:233903.
21. Zhang S, Genov DA, Wang Y, Liu M, Zhang X. Plasmon-induced transparency in metamaterials. Phys Rev Lett. 2008;101:047401.
22. Mccall S, Hahn E. Self-Induced Transparency. Phys Rev. 1969;183:457–85.
23. Slusher RE, Gibbs HM. Self-Induced Transparency in Atomic Rubidium. Phys Rev A. 1972;5:1634.
24. Cai M, Painter O, Vahala KJ. Observation of Critical Coupling in a Fiber Taper to a Silica-Microsphere Whispering-Gallery Mode System. Phys Rev Lett. 2000;85:74.
25. Zhu D, Shao L, Yu M, Cheng R, Desiatov B, Zhang M, Lončar M, et al. Integrated photonics on thin-film lithium niobate. Adv Opt Photon. 2021;13:242–352.
26. Carmon T, Yang L, Vahala KJ. Dynamical thermal behavior and thermal self-stability of microcavities. Opt Express. 2004;12:4742–50.
27. Wong ZJ, Xu YL, Kim J, O'Brien K, Wang Y, Feng L, Zhang X. Lasing and anti-lasing in a single cavity. Nat Photon. 2016;10:796–801.
28. Jalas D, Petrov A, Eich M, Freude W, Renner H. What is — and what is not — an optical isolator. Nat Photon. 2013;7:579–82.
29. Wiersig Jan. Structure of whispering-gallery modes in optical microdisks perturbed by nanoparticles. Phys Rev A. 2011;84:063828.
30. Wiersig Jan. Enhancing the Sensitivity of Frequency and Energy Splitting Detection by Using Exceptional Points: Application to Microcavity Sensors for Single-Particle Detection. Phys Rev Lett. 2014;112:203901.
31. Sweeney WR, Hsu CW, Rotter S, Stone AD. Perfectly Absorbing Exceptional Points and Chiral Absorbers. Phys Rev Lett. 2019;122:093901.
32. Peng B, Zdemir AK, Liertzer M, Chen W, Yang L. Chiral modes and directional lasing at exceptional points. Proc. Natl. Acad. Sci. U.S.A. 2016;113:6845–6850.
33. Soleymani S, Zhong Q, Mokim M, Rotter S, El-Ganainy R, Ozdemir SK. Chiral coherent perfect absorption on exceptional surfaces. Nat Commun. 2022;13:599.
34. Snijder HJ, Frey JA, Norman J, Flayac H, Savona V, Gossard AC. Observation of the unconventional photon blockade. Phys Rev Lett. 2018;121:043601.
35. Yang J, Yuan L, Qin T, Zhang F, Chen Y, Jiang X, Chen X, Fan SH, Wan W. Phonon-induced anomalous gauge potential for photonic isolation in frequency space. Optica. 2021;8:1448–57.
36. Zhu J, Özdemir SK, He L, Yang L. Controlled manipulation of mode splitting in an optical microcavity by two Rayleigh scatterers. Opt Express. 2010;18:23535–43.
37. Gao G, Zhang Y, Zhang H, Wang Y, Huang Q, Xia J. Air-mode photonic crystal ring resonator on silicon-on-insulator. Sci Rep. 2016;6:19999.
38. Wu R, Zhang J, Yao N, Fang W, Qiao L, Chai Z, Lin J, Cheng Y. Lithium niobate micro-disk resonators of quality factors above 10^7. Opt Lett. 2018;43:4116–9.

Publisher's Note